The 4th International Symposium on More Electric Aircraft Technology (MEA 2017)

8–9 November 2017

Thermal analysis of fault-tolerant electrical machines for more electric aircraft applications

Vincenzo Madonna[1], Paolo Giangrande[1], Chris Gerada[1,2], Michael Galea[1,2]

[1]*PEMC Group, University of Nottingham, Nottingham NG7 2RD, UK*
[2]*PEMC Group, University of Nottingham Ningbo China, Ningbo, People's Republic of China*
E-mail: vincenzo.madonna2@nottingham.ac.uk

Published in *The Journal of Engineering*; Received on 10th January 2018; Accepted on 17th January 2018

Abstract: For safety critical applications, electrical machines need to satisfy several constraints, in order to be considered fault-tolerant. In fact, if specific design choices and appropriate control strategies are adopted, fault-tolerant machines can operate safely even in faulty conditions. However, particular care must be taken for avoiding uncontrolled thermal overload, which can cause severe failures. This study describes the thermal modelling of a three-phase, synchronous machine for aerospace applications, analysing the machine's thermal behaviour under open-circuit fault conditions. A particular winding's layout is chosen with the purpose of satisfying fault-tolerance constraints. The winding temperature is evaluated by using a simplified thermal model, which was experimentally validated. Copper and iron losses, necessary for the thermal simulations, are calculated analytically and through electromagnetic finite element analysis, respectively. Finally, an aerospace study case is presented and the machine's thermal behaviour is analysed during both healthy and open-circuit conditions.

1 Introduction

In traditional fuel-powered aircraft, the main task of the engines consists in producing propulsive power by converting the energy stored in the fuel. A percentage of the fuel energy is also used for generating non-propulsive power, namely pneumatic, hydraulic, mechanical, and electric [1].

At the beginning of 1990s, the more electric aircraft (MEA) concept was proposed by the US Air Force. The MEA concept promotes the use of electric power on-board aircraft, in place of pneumatic, hydraulic, and mechanical powers [2, 3]. Electrical machines play a significant role on aircraft that adopt the MEA concept. In fact, electrical machines are used in several applications, such as for driving valves, actuators, pumps, fans etc. Nevertheless, electrical machines for aerospace applications must be characterised by high power density, high reliability, and fault-tolerance capability [4, 5]. A machine topology able to satisfy high power density requirement is the permanent magnet synchronous machine (PMSM). However, the presence of permanent magnets (PMs) is always a source of concern. Since the excitation field is always present, then the machine is always 'on'. In PMSMs, a suitable fault-tolerance level is achieved when the following constraints are met [6]:

(i) physical separation between phases,
(ii) magnetic isolation between phases,
(iii) implicit limiting of fault currents,
(iv) effective thermal isolation between phases,
(v) complete electrical isolation between phases.

Conditions (i)—(iii) are simultaneously satisfied by adopting a concentrated windings with alternated teeth wound (CWAT) layout. Owing to the coils arrangement, the CWAT configuration ensures physical isolation between the phase windings. The winding pattern adopted in the CWAT configuration leads to a high per-unit self-inductance and negligible mutual inductance, which confine the current value in the case of fault [7]. Since each slot contains only coils belonging to the same phase, condition (iv) is also satisfied when CWAT is adopted [8].

Condition (v) is usually very difficult to achieve, mainly due to it being inherently a system-level issue. It can be met by using independent supplies for each machine phase [9]. This approach, known as power segmentation, allows for a true electrical isolation between phases and thus, the machine is able to operate also under extreme fault conditions, such as open- and short-circuit faults [10]. Fig. 1 shows an example of a fault-tolerant PMSM drive using both CWAT configuration and power segmentation, since each phase winding is supplied by a separate H-bridge converter.

In the case of a single-phase open-circuit fault, PMSMs can still deliver the required torque by adopting appropriate control strategies. Generally, these control strategies aim to increase the current in the healthy phases. For this reason, particular care must be taken in order to avoid uncontrolled thermal overload, which may trigger critical damage (e.g. PM demagnetisation, windings insulation breakdown etc.), leading to drive downtime. Hence, machine thermal analysis is required, considering both healthy and faulty conditions. Thermal analysis can be carried out by building a lumped parameter thermal network (LPTN) of the machine under study [11]. This method allows an accurate estimation of the machine's temperature and requires low computational time [12].

This paper is thus focused on the thermal behaviour of a fault-tolerant PMSM for an aerospace application. The machine under study is investigated during both healthy and fault conditions. In particular, the single-phase open-circuit fault condition is analysed through an experimentally validated LPTN. The PMSM design parameters and its LPTN are discussed, along with the LPTN building procedure. Experimental results are then used to validate the predicted LPTN results.

2 PMSM parameters and application

The fault-tolerant PMSM under study is a 30 slots and 28 poles machine, adopting a three-phase CWAT winding configuration.

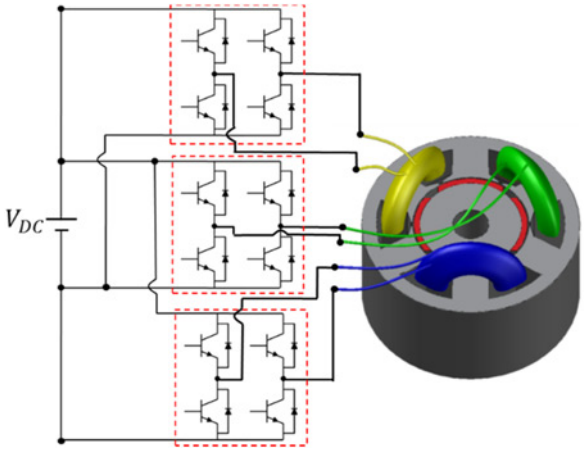

Fig. 1 *Example of fault-tolerant CWAT PMSM drive*

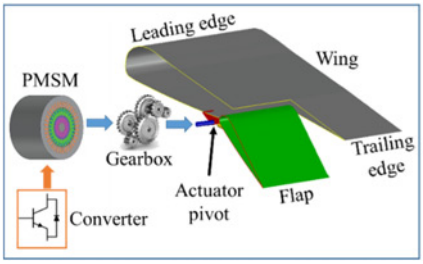

Fig. 2 *Simplified diagram of EMA application*

Each slot contains only one coil's side. This PMSM is designed for a flap control electromechanical actuator (EMA) installed on a medium-sized civil aircraft (e.g. B737 or A320). A simplified diagram of the application, based on the architecture described in [13], is shown in Fig. 2. At the actuator pivot, the application requires a torque of ~30 kN m. Owing to the high torque demanded, the PMSM is coupled to a mechanical gearbox. Indeed, the designed PMSM develops 130 N m at 350 rpm, since a gearbox with 290:1 step-down ratio and 80% efficiency is used. Table 1 reports the main design parameters of the machine, while Fig. 3 shows the geometry and the winding layout.

Although liquid cooled PMSMs reach higher torque density values compared to air-cooled PMSMs, it is desirable to avoid complex cooling infrastructure for aerospace control surfaces applications [4]. For this reason, the designed PMSM is naturally air-cooled. Also, it is important to note that such an application is mainly driven by a short time duty cycle; therefore, the machine is not expected to reach steady-state operation at any point in time.

Table 1 PMSM parameters

slot number (Q)	30
stack length (L)	130 mm
stator outer diameter (D_e)	250 mm
stator inner diameter (D_i)	167 mm
airgap thickness (g)	1 mm
tooth width (Tw)	10.6 mm
yoke thickness (Yt)	12.5 mm
turns per coil (nt)	24
number of strands (ns)	5
single conductor diameter (D_c)	1 mm
wire slot fill factor (ff)	44%
PM material	N35UH
insulation class	180°C (H)
pole number (2p)	28
phase voltage (V_{ph})	110 V rms
rated current (I_n)	28.3 A rms
rated torque (T_n)	130 N m
rated speed (n_n)	350 rpm

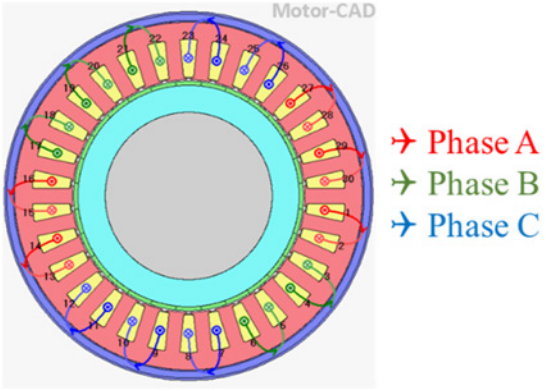

Fig. 3 *Geometry and winding layout of the PMSM under study*

3 PMSM thermal analysis using LPTN

Thermal models are used for predicting the temperature distribution, in order to evaluate the machine's thermal behaviour. Several thermal model topologies, such as computational fluid dynamics (CFDs), finite-element (FE), and LPTNs, can be adopted for the purpose. In this study, the LPTN approach is preferred, due to its lower computational time and good accuracy [12, 14].

In order to identify the PMSM hot-spot and build a simplified LPTN, a preliminary thermal simulation was performed, using the commercial software MotorCAD®. Electromagnetic FE simulations were performed in ANSYS® Maxwell 2D, for determining both the iron and the PM losses to be used in the LPTN. From the FE simulations, the rotor iron losses result two orders of magnitude lower than the stator iron losses. Hence, they can be neglected during the thermal analysis. The PM losses are also negligible, due to the adoption of segmented PMs, which reduces the PMs eddy current losses.

Since both rotor iron losses and PMs eddy current losses provide a small contribute to the PMSM total losses, the rotor is not considered during the thermal analysis. Furthermore, it is reasonable to assume that the rotor is isothermal (at ambient temperature) during short time transient loading, given its considerable thermal inertia [15]. Hence, the simplified LPTN is implemented considering the only stator geometry, while heat sources for both copper and stator iron losses are used. By exploiting the stator symmetry, the LPTN models only one slot and one tooth [11]. In order to build the LPTN, it is necessary to know the thermal properties of the materials, the geometrical dimensions, and the heat transfer coefficients. The analogy between electrical and thermal quantities is reported in Table 2.

The thermal resistances taking into account conduction and convection heat transfer are calculated using (1) and (2), respectively, where l and A are the thermal path length and cross-section area,

Table 2 Thermal and electrical counterparts

Electrical	Thermal
voltage, V	temperature, K
current, A	heat, W
resistance, Ω	resistance, K/W
capacitance, F	capacitance, J/K

while k and h are the thermal conductivity and the convection heat transfer coefficients, respectively

$$R_{\text{cond}} = \frac{l}{k \times A} \tag{1}$$

$$R_{\text{conv}} = \frac{1}{h \times A} \tag{2}$$

Radiation heat transfer is not considered during this study, since its influence is negligible. Transient thermal behaviour is taken into account by including thermal capacitances in the LPTN. These capacitances model the material thermal inertia and they are determined by (3), where c_p is the specific heat capacity and m the body mass

$$C_{\text{th}} = c_p \times m \tag{3}$$

In an LPTN, heat sources, temperature sources, thermal resistances, and capacitances are connected to thermal nodes. A node is defined active when it includes a heat source, while it is passive in case only thermal resistances and/or capacitances form the thermal node. According to the assumptions previously made, the LPTN of the PMSM under study is shown in Fig. 4.

The circumferential heat flow has been considered only in the stator back iron. Fig. 5 shows an example of circumferential path. The cross-sectional area crossed by the heat flow is calculated according to (4), while (5) is used to determine the equivalent thickness of the heat path

$$A = (\text{ro} - \text{ri})L \tag{4}$$

$$t = \frac{\text{ri} + \text{ro}}{2}\varphi \tag{5}$$

Replacing (4) and (5) in (1), the circumferential thermal resistances of the stator back iron (i.e. R_{14}, R_{15}) are obtained, as

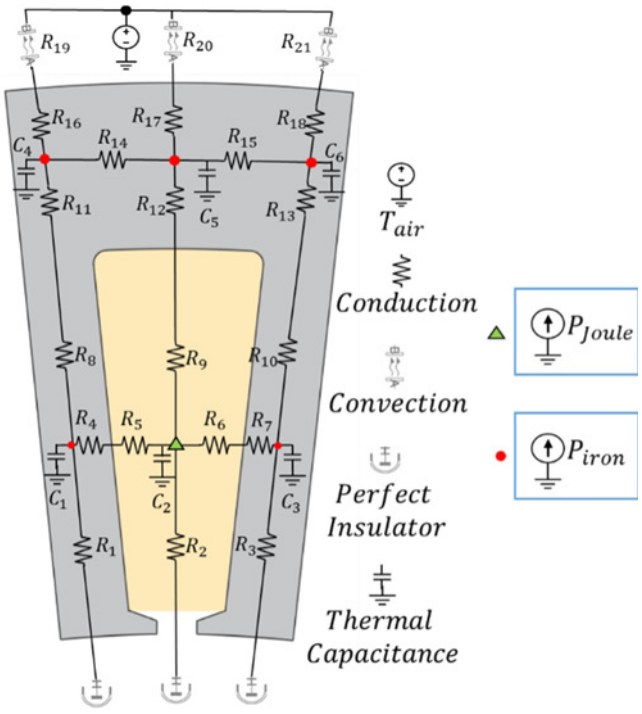

Fig. 4 *Reduced-nodes LPTN*

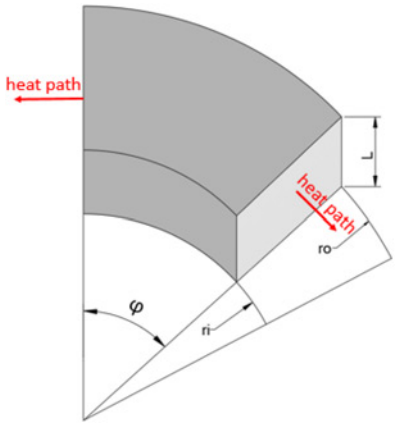

Fig. 5 *Circumferential heat path for stator back iron*

shown in the below equation

$$R_{\text{BackIron}} = \frac{\varphi}{2k_{\text{iron}}L}\frac{\text{ri} + \text{ro}}{\text{ro} - \text{ri}} \tag{6}$$

The radial thermal resistances modelling the slot are obtained assuming the slot geometry as a hexahedron, as depicted in Fig. 6. Introducing the auxiliary variable z (7) and defining the infinitesimal radial resistance (8), the equivalent slot resistances (9) in the radial direction (i.e. R_2, R_9) can be determined by integrating (8)

$$z = B1 + \frac{B2 - B1}{b}x \tag{7}$$

$$\mathrm{d}R_{\text{SlotRad}} = \frac{\mathrm{d}x}{k_{\text{eq}}Lz} \tag{8}$$

$$\begin{aligned} R_{\text{SlotRad}} &= \int_0^b \mathrm{d}R_{\text{SlotRad}} = \frac{1}{k_{\text{eq}}L}\int_0^b \frac{\mathrm{d}x}{\{B1 + [(B2 - B1)/b]\,x\}} \\ &\quad \times \frac{[(B2 - B1)/b]}{[(B2 - B1)/b]} \\ &= \frac{1}{kL[(B2 - B1)/b]} \times \left\{ \ln\left[B1 + \left(\frac{B2 - B1}{\cancel{b}}\right)\cancel{b} \right] - \ln(B1) \right\} \\ &= \frac{1}{kL[(B2 - B1)/b]} \times \ln\left(\frac{\cancel{B1} + B2 - \cancel{B1}}{B1}\right) \end{aligned} \tag{9}$$

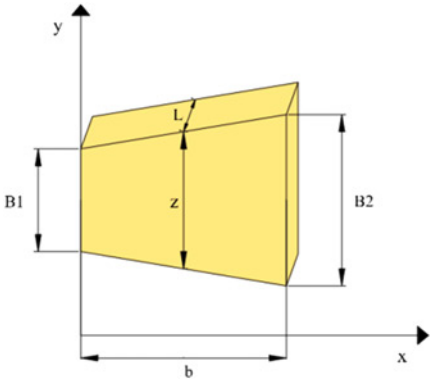

Fig. 6 *Simplified slot shape*

Table 3 Machine's thermal parameters

	Range [17, 18]	Experimental
equivalent slot conductivity	0.5–2 W/(m K)	0.6 W/(m K)
natural air convection coeff.	5–30 W/(m^2 K)	12 W/(m^2 K)
iron conductivity	25–35 W/(m K)	30 W/(m K)
equivalent slot specific heat	400–1k J/(kg K)	430 J/(kg K)
equivalent slot mass density	4–5k kg/m^2	4400 kg/m^2

From a thermal perspective, the slot can be simplistically considered as a compound of two materials, namely copper (conductivity K_{cu}) and impregnating resin (conductivity K_{res}). Therefore, the value of the equivalent slot thermal conductivity is calculated as

$$K_{eq} = K_{res}\frac{(1+ff)K_{cu} + (1-ff)K_{res}}{(1-ff)K_{cu} + (1+ff)K_{res}} \quad (10)$$

A similar approach is used for determining the equivalent thermal capacitance. In particular, the values of the equivalent slot density and specific heat capacity are given by (11) and (12), respectively, where d_{cu} and d_{res} are the copper and resin mass density, respectively, while c_{cu} and c_{res} are the copper and resin specific heat capacity, respectively

$$d_{slot} = d_{cu} \times ff + (1-ff) \times d_{res} \quad (11)$$

$$c_{slot} = c_{cu} \times ff + (1-ff) \times c_{res} \quad (12)$$

Since the slot liner has a thermal conductivity approaching K_{eq}, its resistance is taken into account during the slot thermal modelling.

3.1 Fine tuning the model

Accurate temperature estimation can be obtained by using an LPTN. However, there are some critical parameters, which affect the LPTN accuracy and are difficult to be analytically determined. As discussed in [16], some examples of critical parameters include

- interference gaps between components,
- equivalent slot conductivity,
- convection heat transfer coefficients,
- uncertainty of material properties.

For most of the critical parameters, their range of variation can be found in the literature [17, 18]. These are empirical values based on previous experience. As listed in Table 3, the range of variation might result significantly wide for some critical parameters. Therefore, selecting the appropriate value is not an easy task, also because it will affect the LPTN accuracy. In order to choose an appropriate value while still achieving accurate temperature prediction, the critical parameters are experimentally identified. An instrumented motorette was manufactured, in order to perform experimental tests. The motorette duplicating one-tenth of the PMSM stator is shown in Fig. 7.

The winding temperatures are measured by using six K type thermocouples, distributed in the dummy coil, as reported in Fig. 8. Thermocouple's measurements were also verified adopting a thermographic camera. The tests are performed feeding the dummy coil through a DC power supply.

The fine tuning of the model has been performed using the Simulink Design Optimization™ toolbox. In particular, this tool allows to import and pre-process the experimentally measured temperature, and it performs the estimation of the critical thermal parameters through a non-linear least squares optimisation algorithm. The error function (to be minimised in the optimisation process) is represented by the difference between the hot-spot temperature

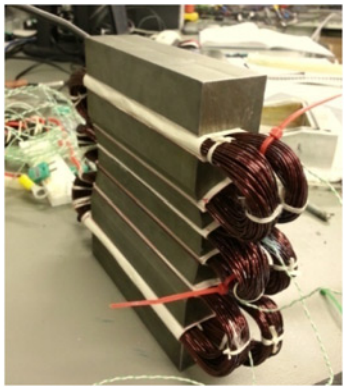

Fig. 7 *Motorette used for experimental tests*

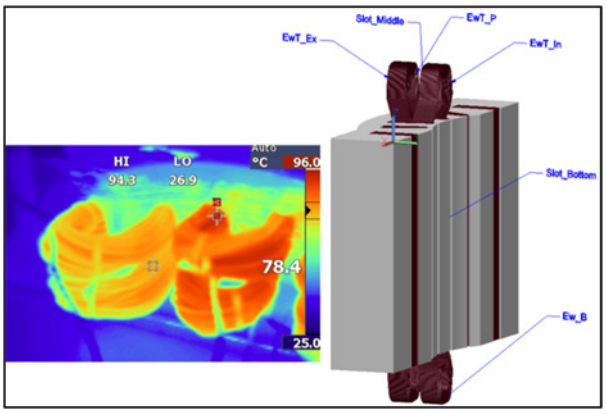

Fig. 8 *K type thermocouples placement and example of infrared thermography*

experimentally measured and the one obtained through the LPTN. Both experimental and predicted hot-spot temperatures are evaluated for various current values.

In Table 3, the critical parameters (experimentally obtained) are compared to their range of variation proposed in the literature, and a good fitting is revealed. The experimental thermal coefficients are adopted, for properly tuning the LPTN. The comparison between experimental and LPTN estimated winding temperature profiles is reported in Fig. 9. In the worst case, the maximum relative error of ~5% is obtained by using the fine-tuned LPTN.

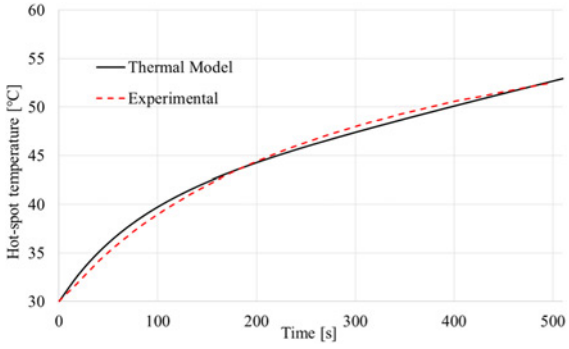

Fig. 9 *Comparison between experimental and LPTN winding temperature profiles*

4 Machine analysis and application

4.1 Healthy operating condition

Once the LPTN is experimentally tuned and validated, it can be used for evaluating the PMSM thermal performances in healthy and single-phase open-circuit conditions. In healthy conditions, the phase current is equal to 28.3 A rms, which corresponds to a current density of 7.2 A/mm^2. In order to determine the copper losses, the electrical resistance of the stator coils is calculated using (13), where l_{coil} is the average length of the turn, N_{turns} the number of turns, S_{cond} the cross-sectional area of the wire, and $\rho_{cu}(T)$ is the copper electrical resistivity at temperature T

$$R_{coil} = \frac{l_{coil} N_{turns}}{s_{cond} \rho_{cu}(T)} \tag{13}$$

Since the resistivity varies with the temperature, it is necessary to iterate the LPTN simulation a few times. The iteration of the thermal simulation is automated by building the LPTN in Simscape™ and monitoring the iteration process by using a purposely built Matlab® script.

The instantaneous value of the electromagnetic torque is obtained through FE simulation using ANSYS® Maxwell 2D. The developed torque at rated current is equal to 137.13 N m (average value), as depicted in Fig. 10. Fig. 11 shows the PMSM's flux lines and magnetic flux density at rated and healthy conditions.

As mentioned earlier, the copper losses are calculated analytically, while the stator iron losses are obtained from FE simulations.

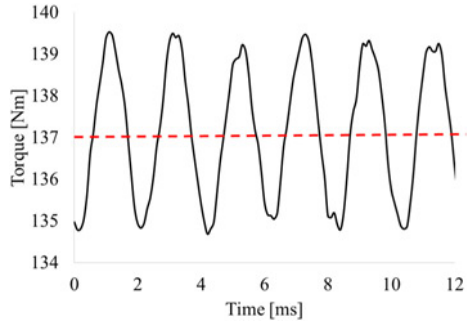

Fig. 10 *Instantaneous and average electromagnetic torque at rated current during healthy condition*

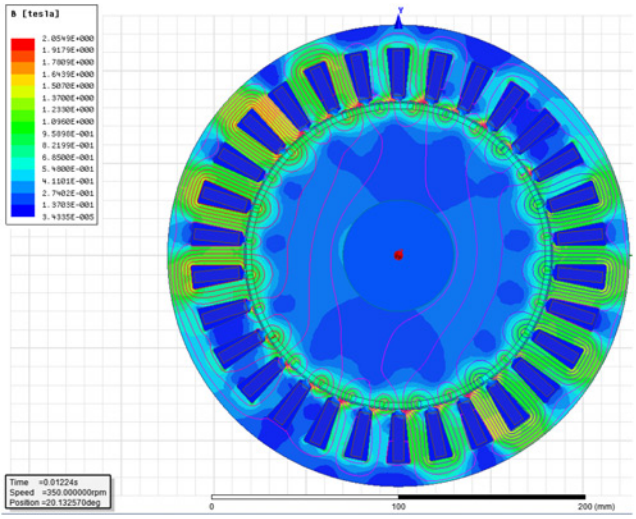

Fig. 11 *Flux lines and magnetic flux density at rated current during healthy condition*

These losses are used for feeding the LPTN, which will estimate the winding temperature in both healthy and single-phase open-circuit conditions. The ambient temperature adopted for the thermal analysis is equal to 70°C, which considers the worst-case scenario for the aerospace application under study.

4.2 Single-phase open-circuit fault

If a single-phase open-circuit fault occurs, a suitable control strategy needs to be implemented, in order to complete the EMA mission. Hence, the required torque needs to be developed also under fault condition. Assuming a single-phase open-circuit on the 'A' phase, the simplest control strategy consists in increasing the current amplitude flowing through the healthy phases by $\sqrt{3}$ and displace their vectors by 30° from the original axis position, as shown in Fig. 12 [19]. In particular, Fig. 12 reports the developed torque and the control strategy in three different operating conditions:

(i) From 0 to 50 ms, the PMSM operates in healthy condition at rated current.
(ii) At 50 ms, the phase '*A*' is open in order to simulate the single-phase open circuit. Thus from 50 to 100 ms, the PMSM operates under fault condition and the compensation control strategy is not implemented.
(iii) At 100 ms, the compensation control strategy is applied. Hence, the PMSM works under fault condition using the compensation control strategy, from 100 to 150 ms.

Implementing the described control strategy, the PMSM is able to develop 135.45 N m (average torque) under fault condition. This average torque satisfies the application requirement, allowing the EMA completing its mission. However, the control strategy adoption increases the PMSM torque ripple compared to the healthy condition.

Table 4 reports both the average torque and torque ripple values, during pre- and post-fault conditions (with and without control strategy implementation). The ratio between actual and rated phase current (I_{ph}/I_n) is also listed in Table 4. It is worth pointing out that the power converter must be designed to handle the

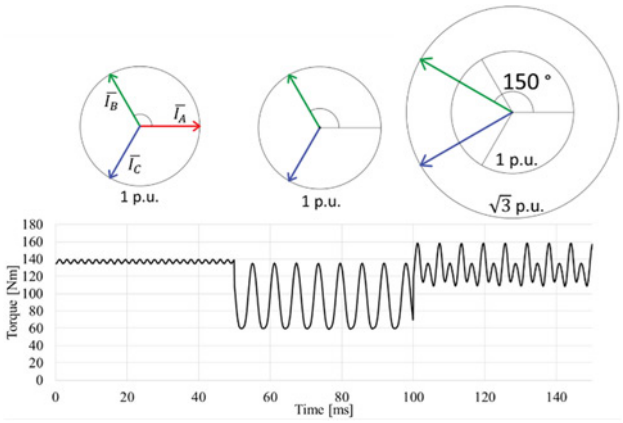

Fig. 12 *Torque and control strategy pre- and post-fault*

Table 4 PMSM performance pre- and post-single-phase open circuit

Operating condition	T_{avg}, N m	Ripple, %	I_{ph}/I_n
healthy (0–50 ms)	137.13	3.5	1
faulty (50–100 ms)	92.36	82.1	1
control strategy (50–150 ms)	135.45	38.6	1.73

doi: 10.1049/joe.2018.0040

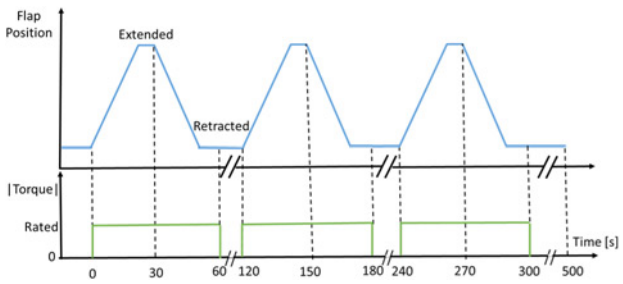

Fig. 13 *Flap mission profile and PMSM torque profile duty cycle*

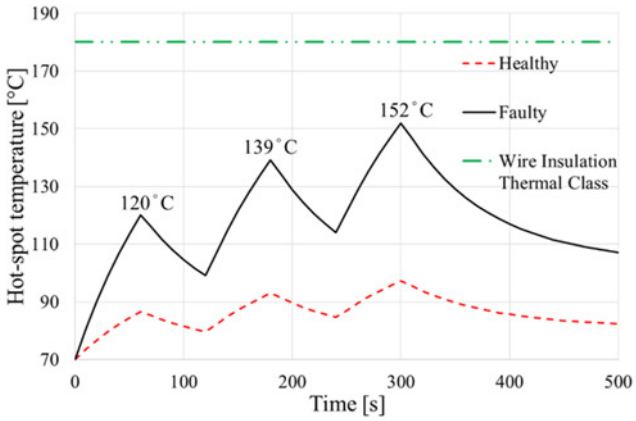

Fig. 14 *PMSM winding temperature profiles in healthy and fault conditions, during EMA mission*

overload condition (i.e. 173% of the rated current), in order to avoid faults after the control strategy implementation.

4.3 Thermal analysis

After performing both the experimental validation of LPTN and PMSM performance analysis in healthy and fault conditions, the LPTN is finally used for predicting the winding temperature. The LPTN might also be used for defining the maximum torque profile achievable, without exceeding the insulation thermal class temperature. Flaps are used in aircraft for increasing the wing's lift during take-off and landing. Hence, the flap EMA is operated only for a small fraction of the total flight time. For a medium-sized civil aircraft, the time necessary for flap extension (or retraction) is usually <30 s. However, for safety reasons, the PMSM must be able to perform three complete cycles (extension + retraction) every 500 s with a rest time of 60 s between each cycle [13]. The flap mission profile aforementioned is provided in Fig. 13 [13] alongside with the PMSM torque profile duty cycle. Fig. 14 reports the winding temperature profile considering the flap EMA mission, in both healthy and faulty operating conditions. The results of Fig. 14 show that the PMSM, driving the flap EMA, can operate also in faulty conditions, without exceeding the thermal class temperature of the wire insulation. Furthermore, it can be observed how the highest temperature reached is well below the maximum allowable temperature of 180°C. This fits well with the general thermal rule of thumb based on the assumption that the location of the highest temperature hot-spot can never be identified exactly and therefore, a safety margin always needs to be considered.

5 Conclusions

In this paper, a fault-tolerant PMSM has been investigated with special focus on its thermal behaviour considering both healthy and single-phase open-circuit conditions. This work focuses its attention on the importance of including thermal analysis at the design stage of fault-tolerant PMSM. The simplified LPTN used for the thermal analysis is presented and discussed. The LPTN is experimentally validated via a custom-built motorette, in order to determine the critical parameters, such as equivalent slot conductivity, convection heat transfer coefficient etc. and achieve better accuracy in temperature prediction. A civil aircraft flap EMA is used as study case for proving the capability of the designed PMSMin working safely under fault conditions. The considerations regarding both thermal modelling and the control strategy in faulty conditions provided along the paper have general validity. Hence, they can be extended to different machine topologies and applications.

6 Acknowledgments

This work is funded by the INNOVATIVE doctoral programme. The INNOVATIVE programme is partially funded by the Marie Curie Initial Training Networks (ITN) action (project number 665468) and partially by the Institute for Aerospace Technology (IAT) at the University of Nottingham.

7 References

[1] Moir I., Seabridge A.: 'Aircraft systems: mechanical, electrical and avionics subsystems integration', vol. **52** (John Wiley & Sons, NJ, USA, 2011)
[2] Rosero J.A., Ortega J.A., Aldabas E., *ET AL.*: 'Moving towards a more electric aircraft', *IEEE Aerosp. Electron. Syst. Mag.*, 2007, **22**, pp. 3–9
[3] Glassock M.G.R., Williams W., Glesk T.: 'Novel hybrid electric aircraft propulsion case studies', *MDPI J. Aeronaut. Astronaut.*, 2017, **4**, (3), Art. no. 45
[4] Gerada C., Galea M., Kladas A.: 'Electrical machines for aerospace applications'. 2015 IEEE Workshop on Electrical Machines Design, Control and Diagnosis (WEMDCD), 2015, pp. 79–84
[5] Barater D., Immovilli F., Soldati A., *ET AL.*: 'Multistress characterization of fault mechanisms in aerospace electric actuators', *IEEE Trans. Ind. Appl.*, 2017, **53**, pp. 1106–1115
[6] Mecrow B.C., Jack A.G., Haylock J.A., *ET AL.*: 'Fault-tolerant permanent magnet machine drives', *IEE Proc. – Electr. Power Appl.*, 1996, **143**, pp. 437–442
[7] Ishak D., Zhu Z.Q., Howe D.: 'Comparison of PM brushless motors, having either all teeth or alternate teeth wound', *IEEE Trans. Energy Convers.*, 2006, **21**, pp. 95–103
[8] Jack A.G., Mecrow B.C., Haylock J.A.: 'A comparative study of permanent magnet and switched reluctance motors for high-performance fault-tolerant applications', *IEEE Trans. Ind. Appl.*, 1996, **32**, pp. 889–895
[9] Bianchi N., Bolognani S., Pre M.D., *ET AL.*: 'Post-fault operations of five-phase motor using a full-bridge inverter'. 2008 IEEE Power Electronics Specialists Conf., 2008, pp. 2528–2534
[10] Bianchi N., Pre M.D., Grezzani G., *ET AL.*: 'Design considerations on fractional-slot faulttolerant synchronous motors'. IEEE Int. Conf. on Electric Machines and Drives, 2005, 2005, pp. 902–909
[11] Sciascera C., Giangrande P., Papini L., *ET AL.*: 'Analytical thermal model for fast stator winding temperature prediction', *IEEE Trans. Ind. Electron.*, 2017, **64**, pp. 6116–6126
[12] Boglietti A., Cavagnino A., Staton D., *ET AL.*: 'Evolution and modern approaches for thermal analysis of electrical machines', *IEEE Trans. Ind. Electron.*, 2009, **56**, pp. 871–882
[13] Bennett J.W., Mecrow B.C., Jack A.G., *ET AL.*: 'A prototype electrical actuator for aircraft flaps', *IEEE Trans. Ind. Appl.*, 2010, **46**, pp. 915–921
[14] Galea M., Gerada C., Raminosoa T., *ET AL.*: 'A thermal improvement technique for the phase windings of electrical machines', *IEEE Trans. Ind. Appl.*, 2012, **48**, pp. 79–87
[15] Boglietti A., Carpaneto E., Cossale M., *ET AL.*: 'Stator-winding thermal models for short-time thermal transients: definition and validation', *IEEE Trans. Ind. Electron.*, 2016, **63**, pp. 2713–2721
[16] Boglietti A., Cavagnino A., Staton D.: 'Determination of critical parameters in electrical machine thermal models', *IEEE Trans. Ind. Appl.*, 2008, **44**, pp. 1150–1159

[17] Tong W.: 'Mechanical design of electric motors' (Taylor & Francis, Abingdon, UK, 2014)
[18] Pyrhonen J., Jokinen T., Hrabovcova V.: 'Design of rotating electrical machines' (John Wiley & Sons, NJ, USA, 2009)
[19] Welchko B.A., Lipo T.A., Jahns T.M., *ET AL.*: 'Fault tolerant three-phase AC motor drive topologies: a comparison of features, cost, and limitations', *IEEE Trans. Power Electron.*, 2004, **19**, pp. 1108–1116